High Yield synthesis of aspect ratio controlled graphenic materials from anthracite coal in supercritical fluids

Suchithra Padmajan Sasikala, Lucile Henry, Gulen Yesilbag Tonga, Kai Huang, Riddha Das, Baptiste Giroire, Samuel Marre, Vincent M. Rotello, Alain Penicaud, Philippe Poulin, et al.

High yield synthesis of aspect ratio controlled graphenic materials from anthracite coal in supercritical fluids

Suchithra Padmajan Sasikala[†], Lucile Henry[†], Gulen Yesilbag Tonga[‡], Kai Huang[§], Riddha Das[‡], Baptiste Giroire[†], Samuel Marre[†], Vincent M. Rotello[‡], Alain Penicaud[§], Philippe Poulin[*§], and Cyril Aymonier[*†]

† CNRS, University of Bordeaux, ICMCB, UPR 9048, Pessac 33600, France
‡ Department of Chemistry, University of Massachusetts, Amherst, Massachusetts 01003, United States
§ Centre de Recherche Paul Pascal, CNRS, University of Bordeaux, Pessac 33600, France

Abstract : This paper rationalizes the green and scalable synthesis of graphenic materials of different aspect ratios using anthracite coal as a single source material under different supercritical environments. Single layer, monodisperse graphene oxide quantum dots (G**QDs**) are obtained at high yield (55 wt %) from anthracite coal in supercritical water. The obtained G**QDs** are ~3 nm in lateral size and display a high fluorescence quantum yield of 28%. They show high cell viability and are readily used for imaging cancer cells. In an analogous experiment, high aspect ratio graphenic materials with ribbon-like morphology (G**Rs**) are synthesized from the same source material in supercritical ethanol at a yield of 6.4 wt %. A thin film of G**Rs** with 68% transparency shows a surface resistance of 9.3 kΩ/sq. This is apparently the demonstration of anthracite coal as a source for electrically conductive graphenic materials.

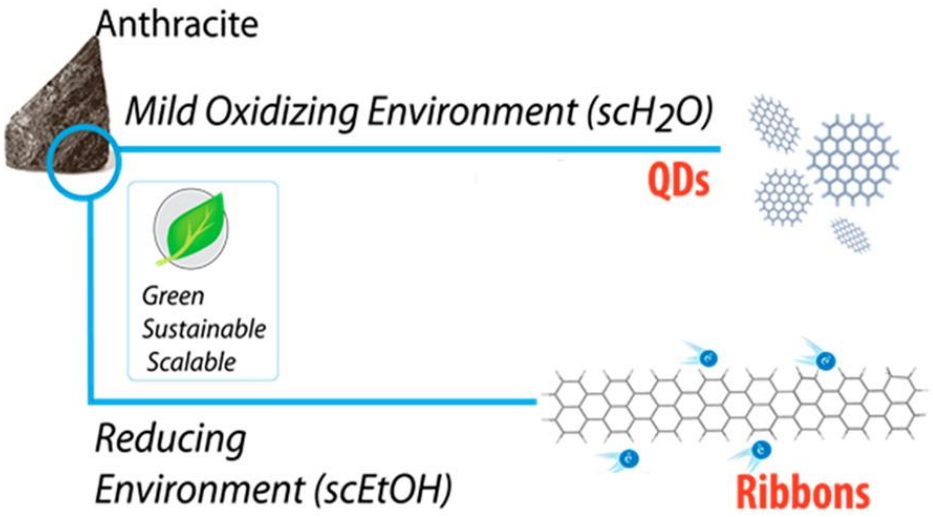

Graphene has been hailed as the miracle material of the 21st century since its in-depth study in 2004 by Novoselov *et al.*(1) Because of its unusual combination of unique properties and technological impact, considerable progress has been achieved recently in the processing of graphene and its associated nanostructures, including graphene based quantum dots and ribbons. This has opened many exciting applications for these materials in optoelectronics, sensing, nanoelectromechanics, thermoelectric devices, and bioimaging, among many others.(2, 3) Adhering to the recommended nomenclature for two-dimensional carbon materials,(4) in this article by referring to G**QDs** and G**Rs**, we mean graphene oxide/reduced graphene oxide quantum dots and ribbons,

respectively. G**QDs** are generally synthesized through solution-based methods such as electrochemical, hydrothermal, acidic oxidation, microwave, and organic synthesis.(5-14) The limiting factors for these existing processes are long treatment times (24–48 h), need for preoxidation steps, and tedious post synthesis purification procedures. In most of the cases, the obtained G**QDs** have broad size distribution, and have limitations on the product purity as well as the quantum yield. G**Rs**, on the other hand, are usually obtained through Chemical Vapor Deposition (CVD) processes, lithographic patterning, sonochemical cutting of graphene, unzipping of carbon nanotubes, and organic synthesis. Only the CVD process has been proven to be scalable for low defect G**Rs**, which however faces difficulties in removing G**Rs** from the surface of metal catalysts.(15-19) In general, classical chemical methods for synthesis of graphenic materials are time-consuming and based on the use of harsh reactants, metal catalysts or ultrasonication.(20) In this scenario, either a scalable and practical production method for graphenic structures with good opical/electrical properties or an identification of cheap sources other than graphite is challenging. If successful, this would advance the industrial applications of graphenic materials even more rapidly.

Coal is a cheap energy source that contains graphitic crystalline domains linked by amorphous carbon chains (Figure S1, Supporting Information). It has been reported that most of the weakest bonds in coal structure can be broken/destroyed by depolymerization reactions including oxidation, pyrolysis, and cationic depolymerization.(21) There have been numerous attempts to degrade the aliphatic portion of coal, while keeping the aromatic structure intact through oxidation, which however often results in degradation of both aliphatic and aromatic domains.(22) Very recently, in a pioneering work, Ye *et al.*(23, 24) reported an oxidation method that comprises ultrasonication and heat treatment of coal in a nitrating mixture at 120 °C for 24 h, followed by dialysis (for ~5 days) and cross-flow ultrafiltration procedures to produce G**QDs**. Similarly, Zhang *et al.*(25) also isolated G**QDs** by refluxing coal in HNO_3 for 24 h, followed by a series of centrifugation, sedimentation, redispersion, and neutralization procedures. In addition to the need for harsh reaction conditions and long post treatment purification procedures, the acid oxidation methods presented by the two groups for coal derived G**QDs** suffer from low product yield(23) and low quantum yield (~2% with quinine sulfate as reference).(25) The development of a scalable method using milder reaction conditions and yet providing different graphene based products with good yield and high quality is desirable to make coal an input for graphenic materials. Coal has an inherent disordered structure compared to graphite, and is thus easier to exfoliate. Selective depolymerization in a controlled atmosphere offered by supercritical fluids could be an appropriate method to have access to graphitic domain without inducing many defects. In this work, we have demonstrated that an oxidizing supercritical fluid (supercritical water, T_c = 374 °C and P_c = 22.1 MPa) treatment can extract highly emissive single layer G**QDs** from coal within 120 min. On the other hand, a reducing supercritical fluid (supercritical ethanol, T_c = 240.9 °C, and P_c = 6.1 MPa) treatment results in electrically conductive G**Rs** within 60 min. Our methodology does not require any preoxidation or post-treatment purification procedures and is scalable for mass production in an environmentally benign way. While this study puts forward a more effective and green alternative process for deriving G**QDs** from coal with enhanced product yield and product quality compared to existing literature, this

is the first report on deriving electrically conductive graphenic structures from coal which is confined only as an energy source until date.

Results and Discussion

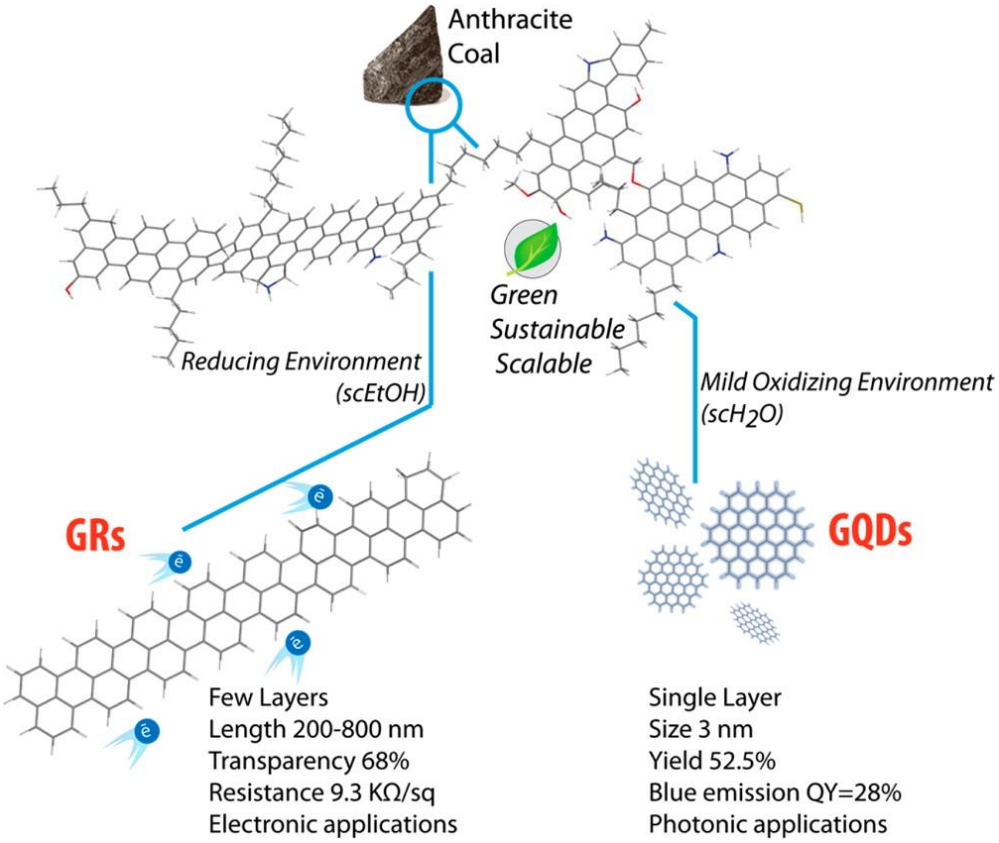

*Scheme 1. Schematic of G**QDs** and G**Rs** Derivation from Anthracite Using Supercritical Fluids as Swelling and Oxidizing/Reducing Media*

Scheme 1 represents the concept of this work showing that controlled oxidation and reduction of anthracite coal lead to selective extraction of highly emissive and electrically conductive graphenic structures, respectively. In this study, anthracite was selected over other coal types due to its lower impurity and high carbon content (>75%).(22) The molecular structure and detailed characterization of anthracite coal used in this study is given in Supporting Information (Figures S1, S2, S3a). Large carbon flakes of heterogeneous size distribution (0.5–8 μm) with crystalline and amorphous domains were observable in high-resolution transmission electron microscopy (HRTEM). The Raman spectrum showed characteristic graphitic D band at 1375.3 cm^{-1} and G band at 1607.5 cm^{-1}. The x-ray photoelectron spectroscopy (XPS) survey showed strong signals of C 1s (~76%), O 1s (~11%), N 1s (~9%), and Na 1s (~4%) (Other impurity elements such as Cl, Se, and F were also seen in trace amount which were disregarded in quantitative elemental analysis). The attenuated total reflectance Fourier transform infrared spectroscopy (FTIR-ATR) spectrum showed the presence of aromatic H-Csp^2 (698 and 3055 cm^{-1}), alkoxy C–O (1063 cm^{-1}), in ring aromatic C–C stretch (1586 cm^{-1}), C═C stretch (1619 cm^{-1}), and O–H (3391 cm^{-1}) vibrations. As a reference experiment, firstly we ultrasonicated anthracite in water and ethanol for 60 min each. The analysis of the resulting products showed that ultrasonication has led to the formation of small

flakes of a few hundred nanometers in size (Figure S3b) with properties similar to that of the starting material. The obtained flakes did not exhibit any observable photoluminescence under excitation with a UV lamp (365 nm). In contrast, supercritical water (scH_2O) treatment of anthracite coal at T = 400 °C and P = 25 MPa for a contact time of 60 min resulted in highly photoluminescent G**QDs-1**. They were found to be stable in water and of lateral size distribution of 4.0–6.0 nm (Figure 1a,b).

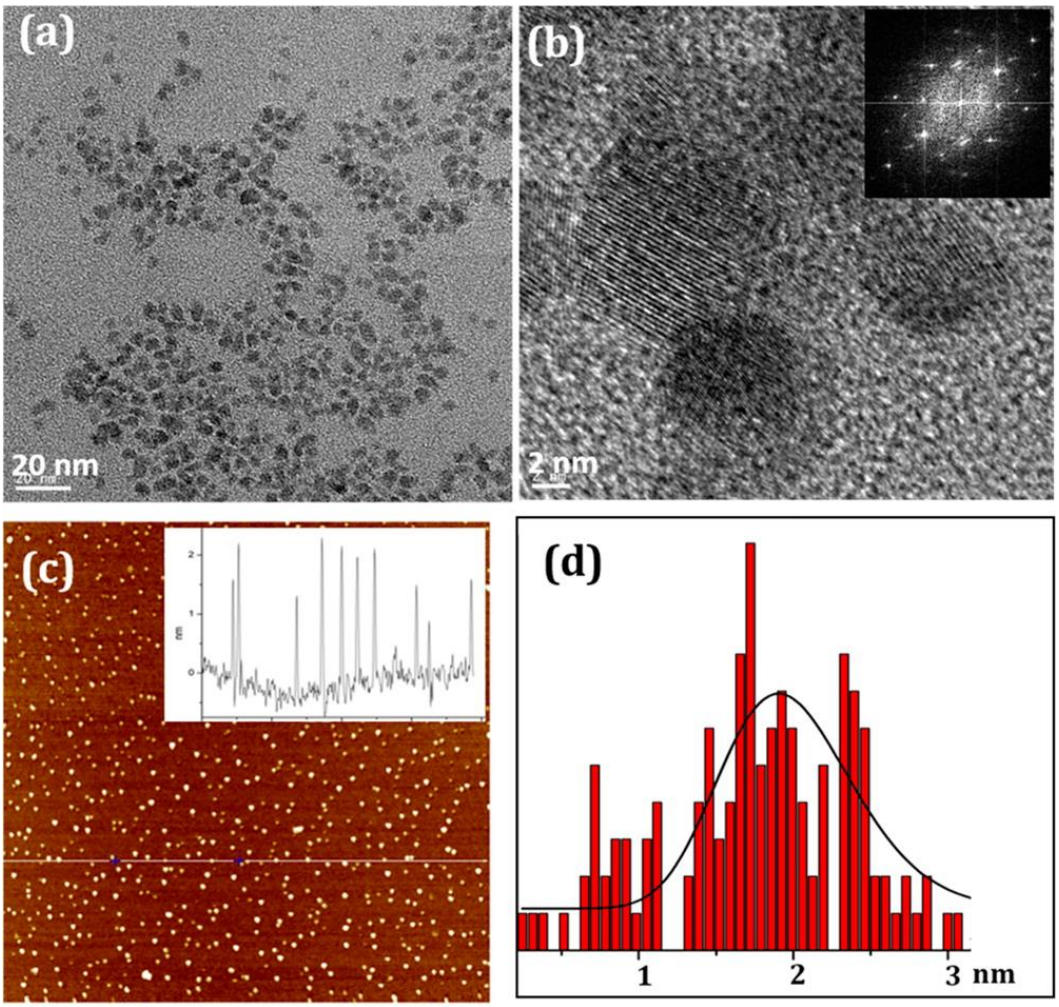

*Figure 1. (a) HRTEM image of G**QDs-1** obtained by supercritical water treatment for 60 min. (b) A magnified HRTEM image displaying graphene fringes. Inset is FFT pattern indicating that the G**QDs-1** are crystalline with a lattice spacing of 0.24 ± 03 nm corresponding to hexagonal graphene lattice fringes. (c) AFM image of GQDs deposited on a mica surface and inset is its height profile along the line drawn. (d) The thickness distribution of the G**QDs-1** in panel c, indicating that the particle thickness is in the range of 0.5–3 nm.*

Most of the particles exhibited <3.0 nm thickness corresponding to six to seven graphene layers (Figure 1c,d). Increasing the contact time of scH_2O with anthracite to 120 min resulted in G**QDs-2**, displaying a narrow size distribution of 2.6 ± 0.4 nm (Figure 2a) in diameter. The HRTEM of single G**QDs-2** particle showed hexagonal unit cell in honeycomb network. The live fast Fourier transform (FFT) image (inset in Figure 2b) showed six spots arranged in a hexagonal pattern with a spacing of 0.21 nm corresponding to the (100) plane of graphene. The average thickness determined by AFM (Figure 2c) was 0.4 ± 0.2 nm corresponding to single layer graphene.(4, 7, 23)

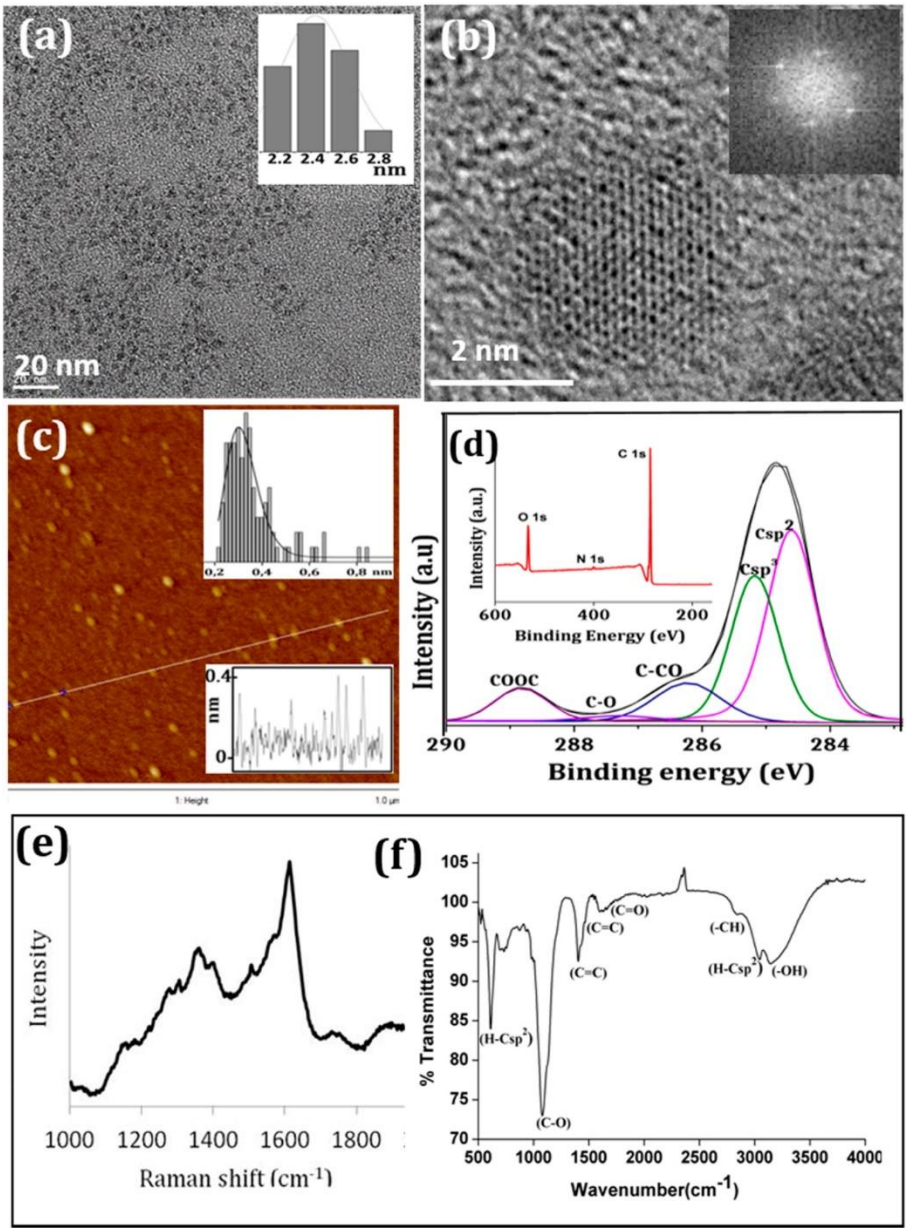

*Figure 2. Characterization of G**QDs-2**: (a) TEM image displaying homogeneous distribution of particles and inset is the size distribution profile. (b) HRTEM image of one G**QDs-2** particle displaying the arrangement of carbon atom in a hexagonal manner. Inset is FFT pattern. (c) AFM image of G**QDs-2** deposited on a mica surface and insets are height distribution and height profile taken along the white line inserted in the image. (d) High-resolution C 1s–XPS spectrum, XPS survey is inset. (e) surface enhanced Raman spectrum of G**QDs-2** deposited on Ag covered SERS substrate under excitation of 638 nm. (f) FTIR-ATR spectrum of G**QDs-2**, obtained after evaporation of water.*

Figure S4 unravels the scH_2O cutting process of anthracite as a function of time from 10 to 120 min. It is interesting to observe that the direct cutting down of large anthracite flakes started as early as 10 min (Figure S4a). However, we could not find any obvious lattice fringes in these quasi-spherical particles (~150 nm). Upon the progress of scH_2O treatment to 30 min, the thickness of carbon spheres decreased significantly. One could clearly observe an arrangement of carbon nanoparticles within each carbon sphere (Figure S4b). The HRTEM image displayed distinguishable graphene lattice fringes with 0.21 nm spacing of nanoparticles which seem to be arranged in random directions within large spheres (of lateral size 115–140 nm). However, domains without any

distinguishable fringes could also be seen. Increasing the treatment time to 60 and 120 min resulted in a homogeneous dispersion of few layered G**QDs-1** and single layered G**QDs-2**, respectively (Figure S4c,d). Both G**QDs-1** and G**QDs-2** displayed crystalline nature (inset of Figure S4c,d). The total product yield achieved after 60 and 120 min of scH_2O treatment is 63.0 and 54.5%, respectively, which are to the best of our knowledge, the highest yield for crystalline G**QDs** reported so far with a top down approach. The light gray and yellow tinted suspension containing G**QDs-1** and G**QDs-2**, respectively, in water were found to be completely stable. The G**QDs-1** and G**QDs-2** could be recovered by evaporation of water, and could be redissolved in other polar solvents such as ethanol, tetrahydrofuran (THF), and dimethylformamide (DMF). However, the as-obtained G**QDs-1** in water suspension displayed slight sedimentation after one month, whereas G**QDs-2** displayed good stability for months. Hence, we investigated further G**QDs-2**, which are single layer G**QDs**. We assume that on the course of time, the oxidative behavior of scH_2O may have introduced more oxygenated functional groups on the G**QDs-2** which may have helped them to be stable in water. The dielectric constant of water drops from 78.5 (at 25 °C) to 6.0 at critical point (374 °C, 22.1 MPa) due to the reduced number of hydrogen bonds. At this point, scH_2O behaves like a nonpolar solvent and induces cleavage of chemical bonds especially the ether and carbon–carbon (C–C) bonds.(26-28) It has been reported that parallel hydrolysis and pyrolysis reactions can occur in scH_2O with molecules containing a saturated carbon attached to a heteroatom containing leaving group.(29) One main conclusion from our understanding about scH_2O is that the high reactivity of scH_2O and the concomitant hydropyrolysis reaction may have led to the depolymerization of coal through C–C bond fission in the carbon lattice. Yet, the scH_2O oxidation appears to be selective and brings about minimum aromatic ring degradation as opposed to the commonly used oxidizing agents, which are drastic and result in degradation of both aromatic and aliphatic components in the coal.(22) In addition, exfoliation effect of scH_2O(30) is confirmed by our results which showed significant reduction in number of layers for the obtained G**QDs** with an increase of the scH_2O treatment time (Figure S4). Given that there was no observable sedimentation in the product after scH_2O treatment of anthracite, we can assume that the amorphous fractions of anthracite were decomposed and only crystalline domains remained intact. This has also been previously reported that the polycyclic compounds with heteroatoms are decomposed to gaseous products such as CO_2, N_2, N_2O during scH_2O treatment.(31) The XPS analysis (Figure 2d) of G**QDs-2** showed no traces of impurity elements compared to initial anthracite precursor (as shown in Figure S2e). The oxidation effect of scH_2O was evident as XPS displayed strong signals of C 1s (85.9%) and O 1s (14.1%), which included fractions of Csp^2 (284.4 eV), Csp^3 (285.2 eV), C–CO (286.1 eV), C–O (287.1 eV), and COOC (288.8 eV) peaks. The COOH contribution (289.8 eV) and N 1s (399.8 eV) signals were negligible. Due to the nanosize of G**QDs-2**, we have studied Surface Enhanced Raman spectrum on a substrate covered by Ag particles, which advocated the presence of graphitic domains (Figure 2e). The ordered G band was more pronounced than disordered D band with an I_D/I_G ratio of 0.321, which was consistent with the above-mentioned HRTEM images and SAED patterns. The FTIR-ATR spectrum of G**QDs-2** (Figure 2f) displayed strong epoxy (C–O–C) groups at 1058 cm^{-1}, weak carbonyl groups (C═O) at 1720 cm^{-1}, and broadened −OH group at 3371 cm^{-1}. We can assume that more epoxy chains and minimum hydroxyl functional groups exist in the G**QDs-2**, as a result of limited oxidation effect of scH_2O.

The absorption and photoluminescence (PL) measurements were carried out with diluted aqueous solution of G**QDs** at a concentration of 0.2 mg/mL. The absorption spectrum of G**QDs-2** showed a prominent absorption peak at 227 nm due to the π–π* transition of C═C and other shoulder peaks at 271 and 320 nm due to n−π* transition within one or several functional groups such as O–C═O, C═O, and C–OH (Figure 3a). The pH of the as-synthesized G**QDs-2** suspension was slightly alkaline (pH 8.2). Decreasing the pH to acidic condition (pH 2.5) did not alter the absorption maxima. However, a slight red shift of absorption peak from 271 to 287 nm was observed for alkaline conditions at pH 13.0. The respective PL-Excitation (PLE) spectrum corresponding to emission at 440 nm showed distinct excitation bands at 261, 304, 386, and 404 nm irrespective of the pH of the G**QDs-2** suspension (Figure 3b). The corresponding PL spectra were found to be stable in all the pH window from 2.5 to 13.0, with an excitation independent peak maxima (Figure 3c–e), unlike many chemically derived G**QDs-2**, for which the emissive centers are free zigzag edge sites.(7, 23, 32-35) Such free zigzag sites (or −COOH functionalized edges) under acidic conditions get protonated and a complex between the zigzag sites and H^+ is formed, making the emissive state inactive in PL.(7, 33) The stable and high PL intensity of G**QDs-2** at pH 2.5 and 8.2 indicated that the free zigzag edge sites were not responsible for the observed PL. However, PL peak maximum was red-shifted at strong alkaline conditions (pH = 13.0), indicating the lowering of the band gap with a slight decrease of the PL intensity compared to that at pH 2.5 and 8.2. The red-shift in alkaline water can be attributed to negatively charged surface due to deprotonation of surface hydroxyl/carboxyl groups. They inhibit the aggregation of the particles. The observed slightly lower PL intensity may have resulted from a slower radiative pathway at higher emission wavelength.(34) Also, we noted that the PL spectra of G**QDs-2** at pH 2.5 and 8.2 split into two strong sharp peaks of comparable intensities at 416 and 440 nm, and a shoulder peak at 468 nm. G**QDs-2** at pH = 13.0 also showed similar PL spectrum splitting into two sharp peaks at 440 and 466 nm, and a shoulder peak at 497 nm. After a detailed correlation of structural characterizations (Figure 2d,f, which indicated the presence of more epoxy chains and minimum hydroxyl/carboxyl functional groups) with optical characterizations (which indicated negligible/small pH influence in the PL intensity), we attribute the peak splitting of G**QDs-2** to the structural rearrangement of graphene induced by chemical functionalities.(36) This speculation is also in agreement with our observation of similar excitation spectra for G**QDs-2** corresponding to different PL emissions regardless of the pH of the medium (Figures 3b and S5). Hence, we assume that excitation of same ground states leads to all observed emissions establishing the role of quantum confinement in the PL of G**QDs-2**.(37) The optical behavior of G**QDs-1** with PL spectrum split was qualitatively similar to that of G**QDs-2**. But a slight red shift of the PL emission at 425 and 444 nm was observed (Figure 4a) indicating again the role of quantum confinement effect. Additional evidence for quantum confinement playing a major role in the PL of G**QDs** was drawn from Tauc plot (Figure 4b). The optical band gaps observed for G**QDs-1** and G**QDs-2** were 3.18 and 3.41 eV, respectively. The increase in band gap with decreasing sizes seen in G**QDs-1** (~6 nm) and G**QDs-2** (~3 nm) reveals quantum confinement effects as the main reason for PL of G**QDs** rather than the functionalized edge sites.(38)

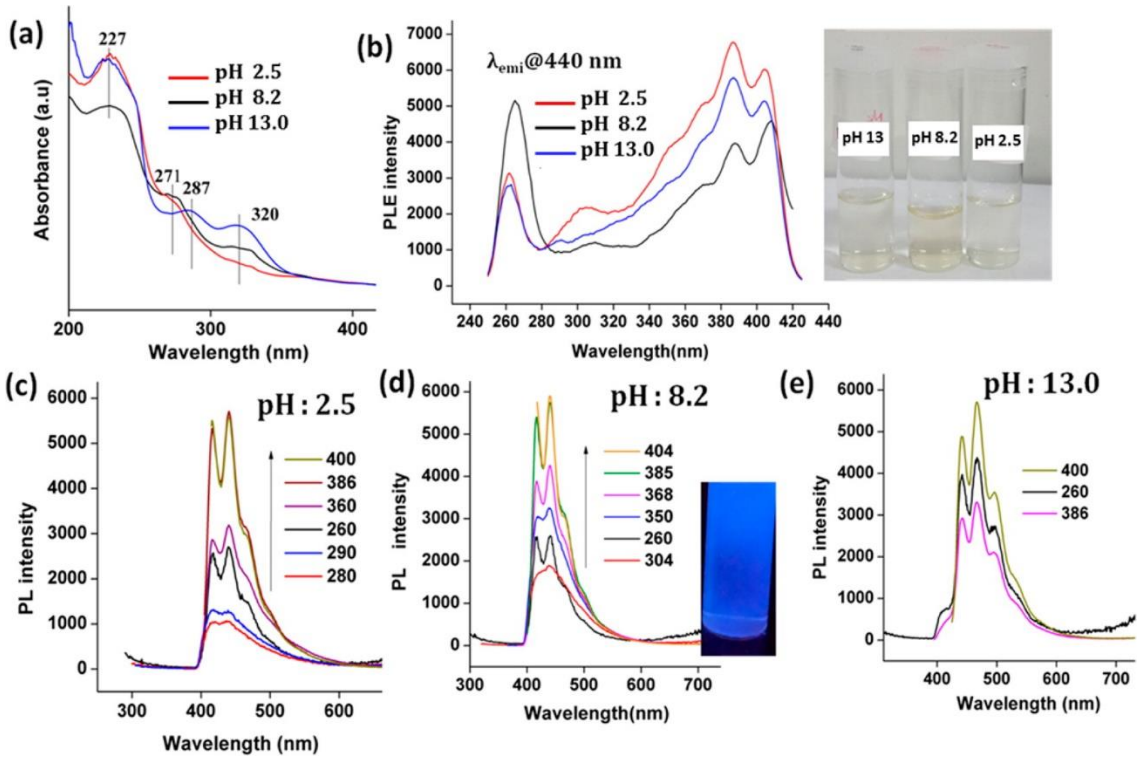

*Figure 3. Optical characterization of G**QDs-2** at different solution pH: (a) UV–visible absorption spectra. (b) PL-excitation spectra and the optical images (on the right) of G**QDs-2** at different pH. PL emission spectra at (c) pH 2.5, (d) pH 8.2, and (e) pH 13.0 for different excitation wavelengths. Inset of (d) is the optical image of G**QDs-2** excited by UV lamp at 365 nm.*

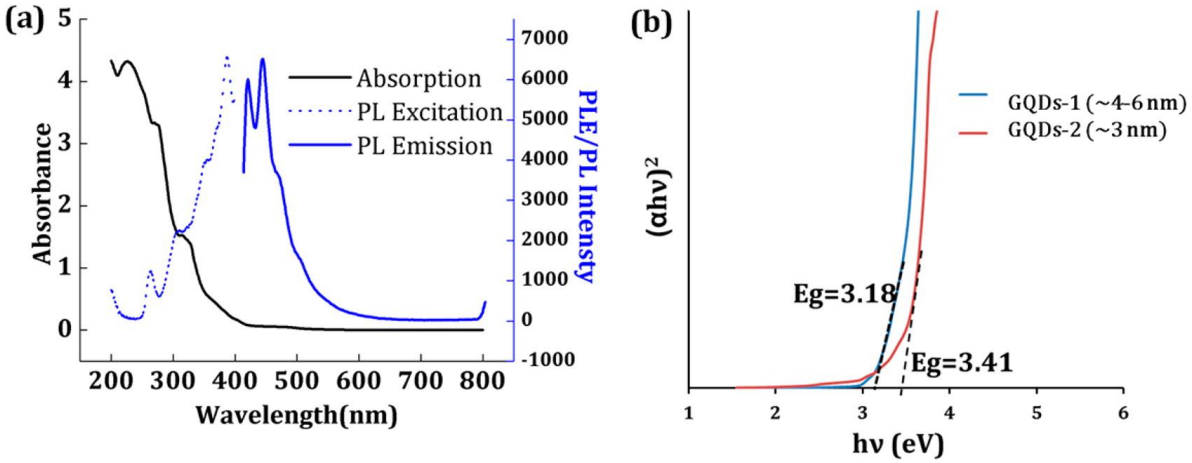

*Figure 4. (a) Combined absorption, PL-excitation (@λem = 425 nm) and PL-emission (@λex = 385 nm) spectra of G**QDs-1**, (b) Tauc plots for G**QDs-1** and G**QDs-2**, which have lateral size of 4–6 and 3 nm, respectively.*

We have done a comparison experiment with natural graphite flakes and supercritical water by repeating the same experimental procedure, that we used for anthracite coal. The recovered product contained large amount of graphite flakes with slight degree of exfoliation (Figure S6a,b). After centrifugation, the recovered top portion of the supernatant showed bright blue fluorescence. The HRTEM showed crystalline G**QDs** (Figure S6c–f). However, the product yield for G**QDs** was calculated to be <4 wt %. This is because the larger and ordered graphite flakes require strong oxidizing conditions (such as HNO_3, H_2SO_4, $KMnO_4$, *etc.*) and shearing effect through ultrasonication to effectively cut down the carbon lattice. The anthracite, on the other hand, could not

withstand such strong oxidizing conditions, if applied, and would end up destroying both aromatic and aliphatic contents. Thus the anthracite requires milder and controllable oxidizing conditions as that of scH_2O. Also of note is that the highly diffusive nature of scH_2O combined with the shearing effect (from stirring) helped in the exfoliation of G**QDs**, and thus results in single layer G**QDs-2**.

Further, we investigated the effect of the reducing supercritical media on coal. The scH_2O in the previous experiments was replaced with scEtOH (solvent grade, 95%) to mimic a reducing environment. The scEtOH at 250 °C is characterized by pronounced hydrogen-bond acidity and weak basicity.(39) For this reason, we can expect less oxidation of coal-carbon lattice with scEtOH. In addition, scEtOH has been proven to exfoliate graphite and well researched for reducing graphene oxide.(40-44) As opposed to scH_2O, the scEtOH treatment of anthracite coal at a temperature of 250 °C and a pressure of 20 MPa for 60 min resulted in dark brown suspension with a low intensity broad fluorescence emission in the range 520–660 nm (Figure S7a,b). After centrifugation–redispersion procedures (see the Experimental Section for details), a precipitate was recovered. High aspect ratio nanostructures of ribbon-like morphology (G**Rs**) were found in high density when this precipitate was analyzed by HRTEM **(**Figure 5a,b) and AFM (Figure 5c,d). We note that along with ribbon-like morphology, some uncut/partially etched sheets and small particles were also seen which remained suspended in ethanol without precipitating out (Figure S8). We assume that in our experiment the less oxidized structures were precipitated during repeated centrifugation–redispersion procedures, while the heavily oxidized nanostructures still remained in the supernatant, which were responsible for the slight fluorescence (Figure S7a,b). The recovered ribbon-like structures were not fluorescent and found with wide range of aspect ratio, *i.e*, 200–800 nm in length and 20–60 nm in width with some degree of aggregation (Figure 5a,b). The selected area diffraction pattern (inset in Figure 5a) showed the bright main spots arranged in a hexagonal pattern and the diffraction intensity of (110) is higher than (210) as expected from graphene.(45, 46) The product yield of recovered G**Rs** is 6.4 wt %, which, considering uncertainties, is comparable with that of sonochemical cutting of graphene sheets (~5 wt %).(16) Note that oxidative unzipping of CNT, although reported to be resulting in higher yield, has the disadvantage of obtaining G**Rs** with higher degree of oxidation, and thus requires heat treatment at >2000 °C to restore the electronic properties.(47) The Raman spectrum (Figure 5e) further demonstrated the graphitic nature of G**Rs** with a well-defined D (1352 nm), G (1565 nm), and 2D (2698 nm) peaks. The calculated I_D/I_G ratio varied from 0.91 to 0.2 in Raman spectra obtained from different spots in the deposited sample on a Si substrate (Figure 5e and Figure S9), which is indicative of breakage of symmetry to an extent either through edges and/or defects introduced by the presence of oxygen groups.(15, 16) Most of the I_D/I_G values calculated for different spots in the sample were between 0.2 and 0.45, and occasionally high I_D/I_G value of 0.91 was observed, which were still less than those for G**Rs** synthesized through sonochemical cutting of graphene sheets, CNT unzipping, or CVD growth ($I_D/I_G > 1.2$).(15, 16, 47) The high-resolution C 1s spectrum from XPS measurements gave Csp^2 (284.5 eV) as major fraction with Csp^3 (285.3 eV) and C–CO (286.3 eV) as minor fractions (Figure 5f), which was consistent with the Raman data that showed evidence of graphenic structure.

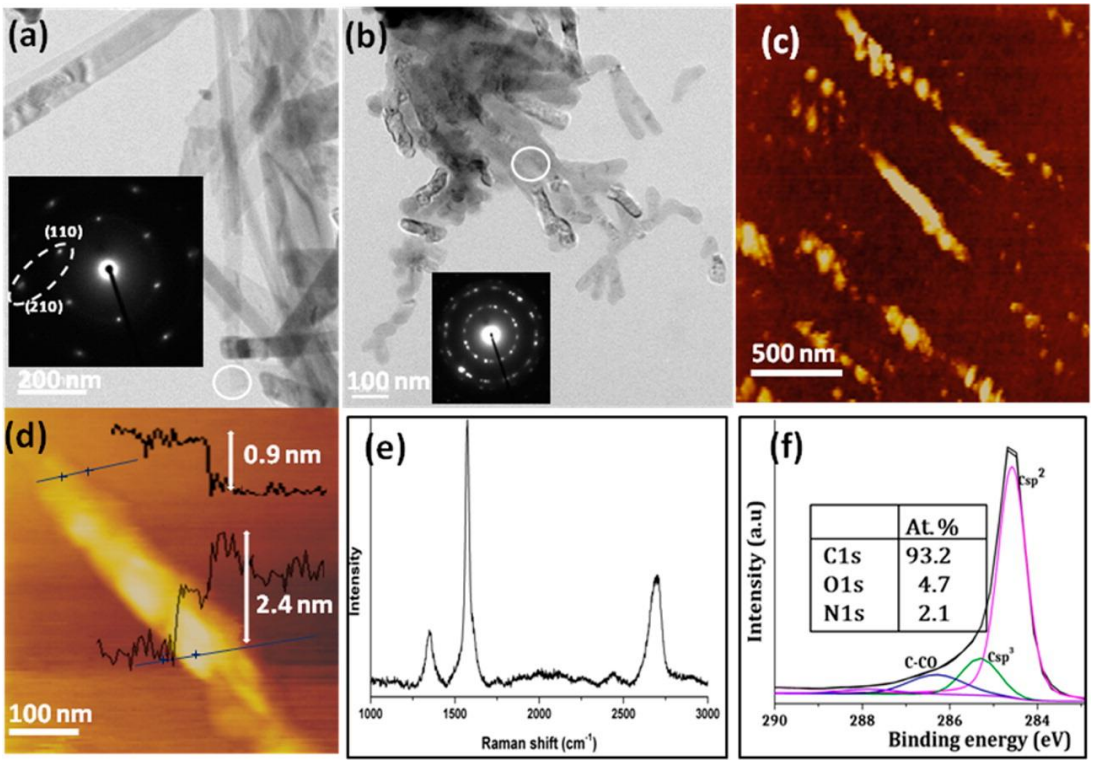

*Figure 5. (a and b) TEM images of G**Rs** with different aspect ratios. Inset is SAED patterns of selected area indicated by white circles. The two spots within white circle in SAED pattern (inset in a) are (01̄10) and (12̄10) planes and are labeled using Miller-Bravais indices (hkil), (c) AFM image of G**Rs** spin coated on a Si/SiO_2 substrate. The G**Rs** sample was ultrasonicated in ethanol for 10 min to disperse the aggregated G**Rs** and immediately spin coated. (d) AFM image of an individual G**R**. Height profiles are given in inset, which indicates layer thickness in the range of 0.9–2.4 nm, confirming few layer nature of G**R**. (e) Raman spectrum and (f) high-resolution C 1s spectrum of G**Rs**. Inset is atomic percentage information obtained from XPS survey.*

Detailed investigation on experimental parameters indicated that besides the temperature and pressure conditions, factors such as solvent purity, starting material, stirring effect, and treatment time have a definite role on the yield and morphology of resulting products. For instance, in the case where there was no stirring, the end products were predominantly large flakes. Similarly, when graphite flakes were used instead of anthracite coal at a temperature of 300 °C for 1 h, we obtained a mixture of exfoliated and unexfoliated graphite flakes and trace amount of G**QDs**. On the other hand, if ethanol/water mixtures were used with anthracite coal at a temperature of 300 °C for 1 h, the product predominantly consisted of blue emissive G**QDs** and small carbon fragments with trace amount of large flakes. The size and emission color could be controlled by difference in the concentration of anthracite, volume ratio of ethanol to water, and treatment time, *etc.* (Figure S10). On the other hand, if absolute ethanol (99.8% purity) was used, predominating product was large flakes similar to the starting anthracite. We have noticed that water, even in trace amount under high temperature–pressure conditions, initiates the cutting of carbon sheets due to its mild oxidizing nature. Li *et al.* reported that low level oxidation induces line defects (fault lines/cracks) in graphite by cooperative alignment of defects especially by the epoxy groups.(48) A following unzipping process triggered by ultrasonication, thermal and/or hydrothermal exfoliation resulted in serial breakage of C–C bonds in a linear mode. The width of the ribbon and edge morphology are generally correlated to the distance between two adjacent line faults and the direction of line faults, respectively.(16) In addition, heteroatoms such as nitrogen present in the carbon lattice are regarded as selective unzipping triggering sites for chemical/electrochemical unzipping of CNT.(49, 50) In the HRTEM analysis of as obtained G**Rs**, parallel regular

morphology was rarely observed; most of the ribbons were seen with irregular edges. It is noteworthy that our scEtOH experiments with graphite as precursor did not give G**Rs**. Similarly, experiments with anthracite coal, but without stirring provided only trace amount of G**Rs**. Considering that the graphite has a quasi-perfect crystalline carbon lattice without any defects and anthracite coal contains considerable oxygen and nitrogen content (Figure S2), we could attribute a combination of factors such as exfoliation effect of supercritical fluids combined with the shearing effect of the stirrer, intrinsic or situational line defects in the anthracite coal, and the heteroatom dopants for the morphology and yield of resulting products. Even though Raman and XPS analysis indicated the graphitic nature of ribbons, a continuous nanometer scale graphene structure is rather unlikely from coal. The detailed HRTEM analysis (Figure 6) indicated a number of randomly arranged different sized crystalline domains inside the ribbon structure. Note that HRTEM provided no evidence of a continuous graphene structure; thus, crystalline domains linked by aliphatic carbon chain may be possibly inferred. Significantly, Kim *et al.* proposed that scEtOH produces α-hydrogen and hydroxyl group which attack the carbon in the epoxy ring and a subsequent proton addition restores the π conjugation by forming $CH_2{=}CH_2$ molecule.(42, 43) In another significant work by Stride *et al.*, gram scale graphene was synthesized using just ethanol and sodium in solvothermal conditions.(51) Under the conditions of closed reactor with heated and pressurized alcohol, ethoxide–ethanol clatherate may formed and trapped ethanol acted as ignition point for the nucleation of sheet, the popcorn effect as called by the authors. The XPS analysis of precursor anthracite coal revealed considerable amount of sodium impurity, and a detailed HRTEM analysis of resulting suspension also revealed agglomerated sheets in trace amount with a tendency to coalesce, in accordance with those of Stride *et al.* (Figure S11).(51) However, these sheets remained suspended in ethanol and were not recovered as precipitate. This may be due to their highly defective nature. The reason for G**Rs** to be precipitated out dominatingly during centrifugation–redispersion procedure can only be reasoned as the absence of many oxygen functionalities which in fact is justified by their aggregated nature as revealed in HRTEM images (Figure 5a,b). There have been a handful of reports on solvothermal graphitization effect in the presence of reductant which led to the synthesis of carbon nanosheets with ordered/disordered graphitic structure.(52-54) In the light of these previous studies, our experimental results and also the graphitic nature of the obtained G**Rs**, we may not disregard the possibility of graphitization contribution from scEtOH.

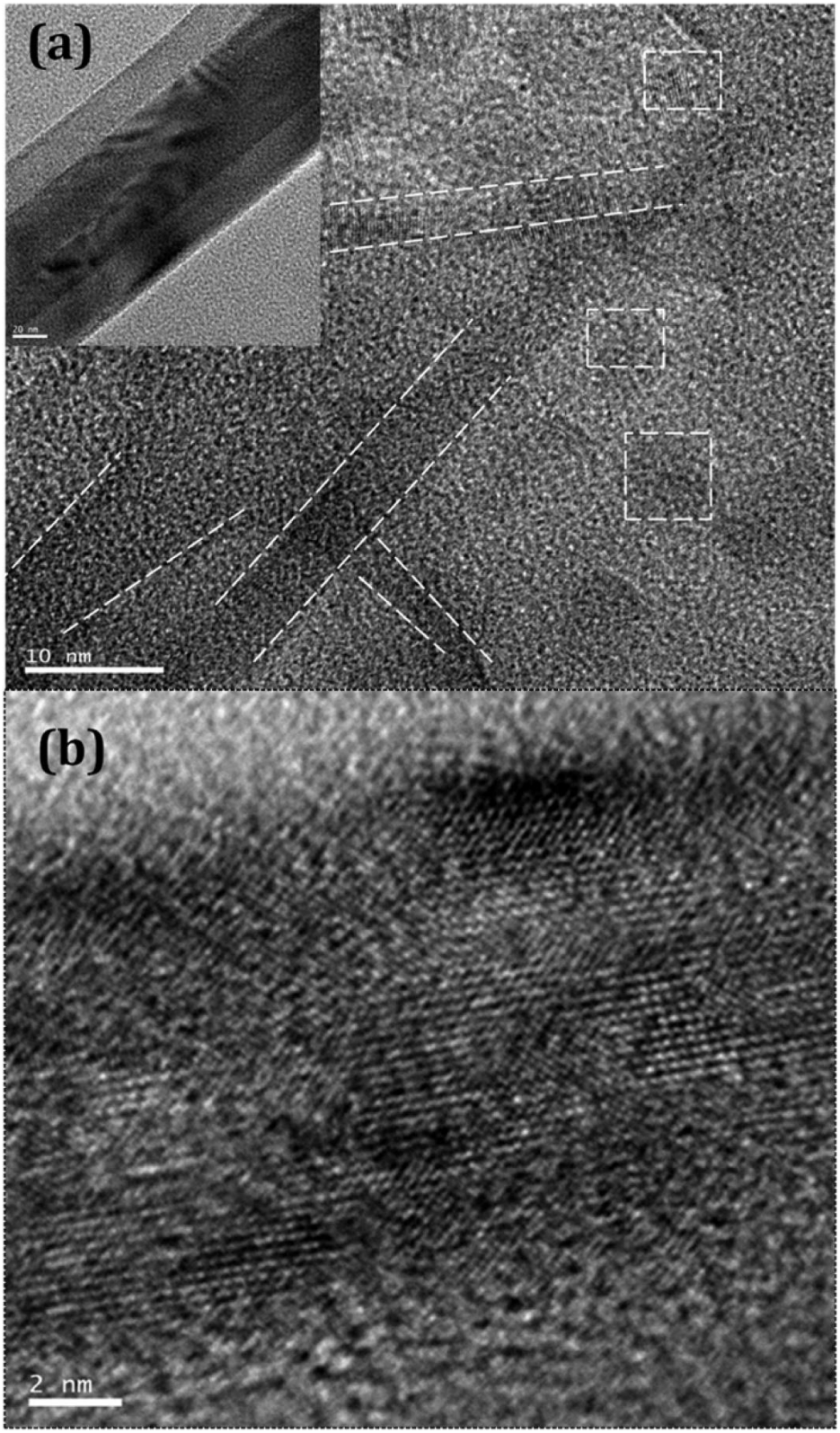

*Figure 6. HRTEM images of **GR** at different magnifications: (a) inset (scale bar 20 nm) is an individual **GR** which is magnified to get the images in (a) and (b). Randomly oriented noncontinuous crystalline domains of different sizes (scale bar 10 nm) with graphene fringes are highlighted in (a). (b) At high-magnifications (scale bar 2 nm), graphene lattice fringes can be discerned.*

In the light of the above discussion, we infer more than one factor to determine the cutting down of coal into graphenic particles of different sizes and aspect ratios. First, the high diffusive nature of supercritical fluids, regardless of their chemical composition, results in exfoliation of the coal. Second, the intrinsic heteroatom doped and disordered crystal structure of coal when combined with the shearing effect from stirring under confined high

temperature and pressure of reactor conditions cut down the large sheets into small fragments. During this scission and exfoliation process, the extent of oxidizing nature of supercritical fluids determines the size and aspect ratio of the obtained graphenic materials. The oxidizing nature of supercritical water causes concomitant hydro-pyrolysis reaction which leads to complete depolymerization of coal sheets. This phenomenon results in small crystalline G**QDs** with small aspect ratio. Also, worthy of note is the fact that increasing the duration of supercritical reaction decreases the number of layers, lateral size, and aspect ratio of obtained G**QDs**. Decrease of aspect ratio can be understood by considering that anisotropic, ribbon shape particles are more likely cut perpendicular to their main axis, resulting in two smaller particles with lower aspect ratio. Cutting perpendicular to the main axis is more likely to arise because of the small length to cut, and because of shear-induced frictional forces are greater along the main axis, in analogy with polymers or rod-like particles.(55-57) Supercritical ethanol has a more pronounced hydrogen bond acidity and weaker basicity than supercritical water. It seems that supercritical ethanol causes cutting of coal through its line defects and heteroatom doped sites. The scission efficiency being weaker than that of supercritical water, the process results in higher aspect ratio graphenic materials with predominantly ribbon-like morphology of few layers. In addition, the reducing nature of supercritical ethanol presumably helps in the graphitization of G**Rs**, which can explain the observed better electrical conductivity. On the other hand, quantum confinement effects and structural rearrangements due to oxygen functionalization together contribute to the optical properties of G**QDs**.

Further, potential applications for our obtained G**QDs-2** and G**Rs** were investigated. The monodisperse G**QDs-2** obtained in water without any stabilizing agents helped them valuable for bioimaging applications. G**QDs-2** showed an excellent quantum yield of 28% measured against quinine sulfate (QS) standard (Figure S12a). Such a high quantum yield is exceptional and cannot be recorded in G**QDs** without surface passivation with polymers.(9-13) However, it should be noted that G**QDs** derived from chemically reduced GO after oxidation in concentrated H_2SO_4 and HNO_3 and an alkaline-hydrothermal deoxidization treatment have been reported to show a maximum quantum yield of 7.5%.(14) This study indeed gave us an indication that selective oxidation induced cutting has a direct correlation to enhance quantum yield. Our selection of coal as a precursor, which has a disordered structure compared to graphite, helped us to overcome the need for many oxidation–reduction steps, as in the case of above mentioned study. We could attribute the high quantum yield of G**QDs-2** to its homogeneous size distribution, and its being the single layer with less defective crystalline lattice. Also G**QDs-2** showed excellent photostability which is comparable to that of quinine sulfate, and much higher than that of CdSe semiconductor QDs (Figure 7a). Such extended stabilities are not associated with surface passivated quantum dots due to the high incidence of optical degradation in the surface functionalities. This in fact rules out the possibility of some surface adsorbed organics on the G**QDs-2**, as a reason for its high quantum yield. High contrast bright cell imaging was possible with our obtained G**QDs-2**. The validation of the potential of the G**QDs-2** is shown in Figure 7b, where the G**QDs-2** have been internalized by HeLa cells into the cytoplasm. The morphology of the cells with phase contrast of nucleus surrounded by blue G**QDs-2** can be clearly visualized. The cell viability studies were performed using different concentrations of as prepared G**QDs-2** (without any

purification) in 10% serum containing media. The Alamar Blue assay indicated no significant toxicity up to the concentration of 40 µg/mL, and <10% toxicity up to 100 µg/mL for an incubation time of 24 h (Figure 7c).

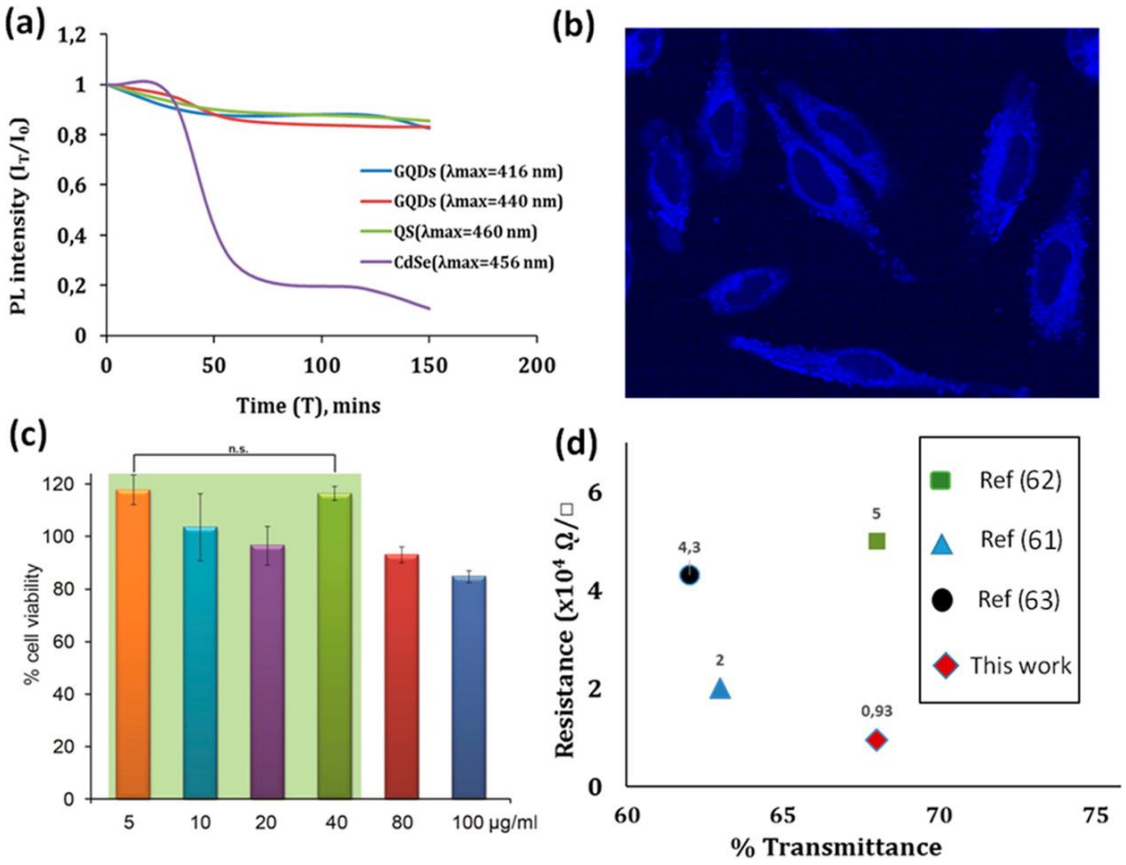

*Figure 7. (a) Photostability comparison of G**QDs-2** with quinine sulfate and CdSe quantum dots prepared in our group as previously reported.(64) (b) Confocal bright field fluorescence image of HeLa cells at 404 nm excitation after 24 h incubation. (c) Cell viability test for HeLa cells incubated with G**QDs** for 24 h. As shown, no significant toxicity (n.s) up to 40 µg/mL (Analysis of variance (ANOVA) p ≥ 0.05). (d) Comparison of surface resistance of G**Rs** film with hydrazine treated and annealed GO films reported in literature which have a comparable transmittance (62–68% at λ = 550 nm).*

The high quantum yield and photostability of G**QDs-2** are distinctive advantages over other QDs for bioimaging and optoelectronic applications such as light emitting diodes at a low concentration. On the contrary, a thin film of G**Rs** deposited on a glass slide showed a surface resistance of 9.3 kΩ/sq with a transparency of 68.2% (at λ = 550 nm, Figure S12b). Such a low resistance compared to G**Rs** made by other methods such as solution phase/plasma unzipping of carbon nanotubes and selective chemical vapor deposition (>1 M Ω/sq) implies high quality of G**Rs** produced by this method.(15, 47, 58-60) This is further confirmed by a correlation study of transparency and surface resistance of obtained G**Rs** compared to high temperature annealed and hydrazine reduced graphene oxide films (Figure 7d).(61-63) As in the case of other synthetic methods, challenges such as uniform edges and stable suspension demand more systematic study on varying supercritical fluids reaction conditions in the future. These results will open avenues toward potential wider application in electrically conductive composite materials where scalable production is more relevant than edge uniformity. Our proposed supercritical fluid method puts forward a new direction for tailoring the morphology of graphenic materials if

combined with the right precursor. This study initiates further investigations to fully understand and resolve the reaction mechanism behind the effect of supercritical/solvothermal conditions on carbon materials. Nevertheless, this is the first demonstration of the proof of concept concerning the effect of two common solvents, water and ethanol, on a highly ranked coal (*i.e.*, anthracite coal), when treated in a closed container above the critical point. Future work is focused on surface modification of G**QDs** and their application in photonics and biomedical science, while optimizing reaction conditions to increase the G**Rs** production yield and its full application in electronic devices.

Conclusion

In conclusion, we report for the first time the supercritical fluid synthesis of aspect ratio controlled graphenic materials from coal. The morphology and electronic properties of obtained G**QDs** and G**Rs** are greatly influenced by the supercritical solvent of synthesis. The ability to tailor the size, structure, and the properties of graphenic materials from anthracite coal with an oxidizing or a reducing environment offered by scH_2O and scEtOH, respectively, is demonstrated. No strong acid treatments, delicate synthetic conditions, long reaction time, sonication, or extensive post treatment purification procedures were required for extracting G**QDs** and G**Rs** from coal. The obtained G**QDs** showed high PL quantum yield of 28% measured against quinine sulfate standard. They displayed good biocompatibility and was readily used to image cancer cells. G**Rs** showed high electrical conductivity (9.3kΩ/sq) for an optical transparency of 68%, which opens up a new direction for coal as a source material for electrically conductive graphenic materials. The supercritical fluid based process is sustainable, versatile, and scalable, thus paving the way to large-scale production of these materials.

Experimental Section

Synthesis of GQDs

Sixty milligrams of anthracite (Fisher Scientific, catalogue number S98806) was suspended in 60 mL of water, and loaded into a batch reactor of total 360 mL capacity. The stirred vessel reactor (Max: 30 MPa, 550 °C) with an Inconel liner and stirrer (95 N·cm) is from Top Industrie (17652000) and equipped with 4 blades with an inclination of 45° in Inconel). The reactor is heated to 400 °C. The internal pressure of the reactor reached 25 MPa when temperature of water reached 400 °C. The anthracite was allowed to swell in supercritical water for a maximum contact time of 120 min with constant stirring (200 rpm). The reactor was then cooled down naturally after the reaction was stopped. The sample was initially dialyzed in a dialysis bag (0.5–1 kDa, Spectrum Labs, product number G235063) for 5 days, but we did not observe any effect of purification in the surface characteristics or optical properties of G**QDs**. All the results shown in this study (including cytotoxicity and bioimaging) are with as prepared G**QDs**, without any purification steps, but centrifuged once (7000 rpm, 30 min) to remove any large flakes if present. For comparison experiments, the procedure was repeated with natural graphite keeping all other conditions the same.

Synthesis of GRs

The procedure described above was repeated with 50 mL of ethanol in a reactor of 80 mL capacity and heated to 250 °C and 20 MPa to reach the supercritical conditions. The reactor (Max: 30 MPa, 250 °C) from Autoclave Engineers is equipped with a stirrer consisting of radial flow impeller with 6 blades (74.6 N·cm) from Maxon Motor (2260.815-51.216-2). All the components are in stainless steel. After 60 min of contact with a stirring speed of 200 rpm, the reactor was rapidly cooled by immersing into the ice cold water. The obtained dark brown suspension was centrifuged and the precipitate was redispersed in fresh ethanol. This process was continued for at least six times. The G**Rs** were finally recovered in powder form by vacuum filtration. The comparison experiment with ethanol–water mixture used the same reactor and experimental conditions. The optical and TEM measurements were done with supernatant of centrifuged sample at 7000 rpm for 60 min.

Bioimaging

HeLa cells were grown in a cell culture flask using low-glucose Dulbecco's modified Eagle medium supplemented with 10% fetal bovine serum at 37 °C in a humidified atmosphere of 5% CO_2. For confocal analysis, HeLa cells were seeded at 200 000 cells (1 mL 10% serum containing media) in the confocal dish 24 h before the experiment. During the experiment, old media were replaced by 100 μg/mL of the G**QDs** (1 mL) in serum-containing media, and the cells were incubated for 24 h. The cells were then washed with PBS three times. Confocal microscopy imaging was performed on a Nikon A1R laser scanning confocal microscope equipped with a Nikon Ti Eclipse microscope and a spectrum detector. The diode lasers were used for illumination with wavelength of 405 nm.

Cytotoxicity Measurements of GQDs

HeLa cells were seeded at 200 000 in 1 mL per well in 12-well plates 24 h before the experiment. Cells were washed with PBS buffer and then treated with 6 different concentrations ranging from 5 to 100 μg/mL of G**QDs** in triplicate. After 24 h of incubation, the cells were then completely washed off with PBS buffer three times, and 10% Alamar Blue in serum-containing media was added to each well (1 mL) and further incubated at 37 °C for 1 h. Cell viability was then determined by measuring the fluorescence intensity (λ_{ex} = 560 nm and λ_{em} = 590 nm) using a SpectraMax M5 microplate spectrophotometer. Further characterization techniques are given in detail as Supporting Information.

Associated Content

The Supporting Information is available free of charge on the ACS Publications website at DOI: 10.1021/acsnano.6b01298.

S1: Characterization techniques. S2: Preparation of thin film of G**Rs**. Figure S1: Representative molecular structure of anthracite coal. Figure S2: Characterization of anthracite coal. Figure S3: (a) FTIR-ATR of anthracite coal, (b) TEM of anthracite coal after ultrasonication in water for 60 min. Figure S4: Supercritical water cutting of anthracite coal into G**QDs** as a function of time. Figure S5: PL-excitation spectra of G**QDs-2** corresponding to different emission wavelengths. Figure S6: Comparison experiment to show the effect of scH_2O treatment on natural graphite flakes. Figure S7: PL- excitation spectrum of the product obtained after anthracite coal was treated with scEtOH. Figure S8: HRTEM analysis of sample obtained from scEtOH treatment of anthracite coal for 60 min. Figure S9: Raman spectra of as obtained G**Rs** deposited on a Si substrate. Figure S10: Effect of ethanol–water mixture on anthracite coal at 250 °C and 20 MPa. Figure S11: TEM images with different magnifications of a sheet structure obtained after scEtOH treatment of anthracite coal. Figure S12: (a) Quantum Yield (QY) calculation for G**QDs-2** with respect to quinine sulfate standard, (b) transmittance% of G**Rs** film on the surface of glass slide (PDF)

Author Information : corresponding : Philippe Poulin - Centre de Recherche Paul Pascal, CNRS, University of Bordeaux, Pessac 33600, France; Email: poulin@crpp-bordeaux.cnrs.fr / Cyril Aymonier - CNRS, University of Bordeaux, ICMCB, UPR 9048, Pessac 33600, France; Email: cyril.aymonier@icmcb.cnrs.fr

Notes : The authors declare no competing financial interest.

Acknowledgment : S.P.S. is thankful to University of Bordeaux and the IdEx postdoctoral fellowship. This work has received financial support from the French State in the frame of the “Investments for the future” Programme IdEx Bordeaux, reference ANR-10-IDEX-03-02 and from the National Institutes of Health (GM077173).

References

1. Novoselov, K. S.; Geim, A. K.; Morozov, S. V.; Jiang, D.; Zhang, Y.; Dubonos, S. V.; Grigorieva, I. V.; Firsov, A. A. Electric Field Effect in Atomically Thin Carbon Films Science **2004**, 306, 666– 669 DOI: 10.1126/science.1102896
2. Shen, J.; Zhu, Y.; Yang, X.; Li, C. Graphene Quantum Dots: Emergent Nanolights for Bioimaging, Sensors, Catalysis and Photovoltaic Devices Chem. Commun. **2012**, 48, 3686– 3699 DOI: 10.1039/c2cc00110a
3. Terrones, M.; Botello-Méndez, A. R.; Campos-Delgado, J.; López-Urías, F.; Vega-Cantú, Y. I.; Rodríguez-Macías, F. J.; Elías, A. L.; Muñoz-Sandoval, E.; Cano-Márquez, A. G.; Charlier, J.-C.; Terrones, H. Graphene and Graphite Nanoribbons: Morphology, Properties, Synthesis, Defects and Applications Nano Today **2010**, 5, 351– 372 DOI: 10.1016/j.nantod.2010.06.010

4. Bianco, A.; Cheng, H. M.; Enoki, T.; Gogotsi, Y.; Hurt, R. H.; Koratkar, N.; Kyotani, T.; Monthioux, M.; Park, C. R.; Tascon, J. M.; Zhang, J. All in the Graphene Family–A Recommended Nomenclature for Two-Dimensional Carbon Materials Carbon **2013**, 65, 1– 6 DOI: 10.1016/j.carbon.2013.08.038
5. Shi, B.; Zhang, L.; Lan, C.; Zhao, J.; Su, Y.; Zhao, S. One-Pot Green Synthesis of Oxygen-Rich Nitrogen-Doped Graphene Quantum Dots and Their Potential Application in Ph-Sensitive Photoluminescence and Detection of Mercury(II) Ions Talanta **2015**, 142, 131– 139 DOI: 10.1016/j.talanta.2015.04.059
6. Baker, S. N.; Baker, G. A. Luminescent Carbon Nanodots: Emergent Nanolights Angew. Chem., Int. Ed. **2010**, 49, 6726– 6744 DOI: 10.1002/anie.200906623
7. Pan, D.; Zhang, J.; Li, Z.; Wu, M. Hydrothermal Route for Cutting Graphene Sheets into Blue-Luminescent Graphene Quantum Dots Adv. Mater. **2010**, 22, 734– 738 DOI: 10.1002/adma.200902825
8. Feng, L.; Tang, X.-Y.; Zhong, Y.-X.; Liu, Y.-W.; Song, X.-H.; Deng, S.-L.; Xie, S.-Y.; Yan, J.-W.; Zheng, L.-S. Ultra-Bright Alkylated Graphene Quantum Dots Nanoscale **2014**, 6, 12635– 12643 DOI: 10.1039/C4NR03506B
9. Prasannan, A.; Imae, T. One-Pot Synthesis of Fluorescent Carbon Dots from Orange Waste Peels Ind. Eng. Chem. Res. **2013**, 52, 15673– 15678 DOI: 10.1021/ie402421s
10. Li, L.; Wu, G.; Yang, G.; Peng, J.; Zhao, J.; Zhu, J.-J. Focusing on Luminescent Graphene Quantum Dots: Current Status and Future Perspectives Nanoscale **2013**, 5, 4015– 4039 DOI: 10.1039/c3nr33849e
11. Li, L.-L.; Ji, J.; Fei, R.; Wang, C.-Z.; Lu, Q.; Zhang, J.-R.; Jiang, L.-P.; Zhu, J.-J. A Facile Microwave Avenue to Electrochemiluminescent Two-Color Graphene Quantum Dots Adv. Funct. Mater. **2012**, 22, 2971– 2979 DOI: 10.1002/adfm.201200166
12. Zhu, S.; Zhang, J.; Tang, S.; Qiao, C.; Wang, L.; Wang, H.; Liu, X.; Li, B.; Li, Y.; Yu, W.; Wang, X.; Sun, H.; Yang, B. Surface Chemistry Routes to Modulate the Photoluminescence of Graphene Quantum Dots: From Fluorescence Mechanism to Up-Conversion Bioimaging Applications Adv. Funct. Mater. **2012**, 22, 4732– 4740 DOI: 10.1002/adfm.201201499
13. Shen, J.; Zhu, Y.; Yang, X.; Zong, J.; Zhang, J.; Li, C. One-Pot Hydrothermal Synthesis of Graphene Quantum Dots Surface-Passivated by Polyethylene Glycol and Their Photoelectric Conversion Under Near-Infrared Light New J. Chem. **2012**, 36, 97– 101 DOI: 10.1039/C1NJ20658C
14. Pan, D.; Guo, L.; Zhang, J.; Xi, C.; Xue, Q.; Huang, H.; Li, J.; Zhang, Z.; Yu, W.; Chen, Z.; Li, Z. Cutting sp^2Clusters in Graphene Sheets into Colloidal Graphene Quantum Dots with Strong Green Fluorescence J. Mater. Chem. **2012**, 22, 3314– 3318 DOI: 10.1039/c2jm16005f
15. An, H.; Lee, W.-G.; Jung, J. Synthesis of Graphene Ribbons Using Selective Chemical Vapor Deposition Curr. Appl. Phys. **2012**, 12, 1113– 1117 DOI: 10.1016/j.cap.2012.02.005
16. Wu, Z.-S.; Ren, W.; Gao, L.; Liu, B.; Zhao, J.; Cheng, H.-M. Efficient Synthesis of Graphene Nanoribbons Sonochemically Cut from Graphene Sheets Nano Res. **2010**, 3, 16– 22 DOI: 10.1007/s12274-010-1003-7
17. Yang, X.; Dou, X.; Rouhanipour, A.; Zhi, L.; Räder, H. J.; Müllen, K. Two-Dimensional Graphene Nanoribbons J. Am. Chem. Soc. **2008**, 130, 4216– 4217 DOI: 10.1021/ja710234t
18. Yu, W. J.; Chae, S. H.; Perello, D.; Lee, S. Y.; Han, G. H.; Yun, M.; Lee, Y. H. Synthesis of Edge-Closed Graphene Ribbons with Enhanced Conductivity ACS Nano **2010**, 4, 5480– 5486 DOI: 10.1021/nn101581k
19. Jiao, L.; Wang, X.; Diankov, G.; Wang, H.; Dai, H. Facile Synthesis of High-Quality Graphene Nanoribbons Nat. Nanotechnol. **2010**, 5, 321– 325 DOI: 10.1038/nnano.2010.54
20. Skaltsas, T.; Ke, X.; Bittencourt, C.; Tagmatarchis, N. Ultrasonication Induces Oxygenated Species and Defects onto Exfoliated Graphene J. Phys. Chem. C **2013**, 117, 23272– 23278 DOI: 10.1021/jp4057048
21. Meyers, R. Coal Structure; Elsevier, 2012.
22. Davidson, R. M. Molecular Structure of Coal Coal Science **1982**, 1, 83– 160 DOI: 10.1016/B978-0-12-150701-5.50009-7
23. Ye, R.; Xiang, C.; Lin, J.; Peng, Z.; Huang, K.; Yan, Z.; Cook, N. P.; Samuel, E. L. G.; Hwang, C.-C.; Ruan, G.; Ceriotti, G.; Raji, A.-R. O.; Martí, A. a.; Tour, J. M. Coal as an Abundant Source of Graphene Quantum Dots Nat. Commun. **2013**, 4, 2943– 2943 DOI: 10.1038/ncomms3943
24. Ye, R.; Peng, Z.; Metzger, A.; Lin, J.; Mann, J. a.; Huang, K.; Xiang, C.; Fan, X.; Samuel, E. L. G.; Alemany, L. B.; Martí, A. a.; Tour, J. M. Bandgap Engineering of Coal-Derived Graphene Quantum Dots ACS Appl. Mater. Interfaces **2015**, 7, 7041– 7048 DOI: 10.1021/acsami.5b01419

25. Dong, Y.; Lin, J.; Chen, Y.; Fu, F.; Chi, Y.; Chen, G. Graphene Quantum Dots, Graphene Oxide, Carbon Quantum Dots and Graphite Nanocrystals in Coals Nanoscale **2014**, 6, 7410– 7415 DOI: 10.1039/c4nr01482k
26. Bröll, D.; Kaul, C.; Krämer, A.; Krammer, P.; Richter, T.; Jung, M.; Vogel, H.; Zehner, P. Chemistry in Supercritical Water Angew. Chem., Int. Ed. **1999**, 38, 2998– 3014 DOI: 10.1002/(SICI)1521-3773(19991018)38:20<2998::AID-ANIE2998>3.3.CO;2-C
27. Saisu, M.; Sato, T.; Watanabe, M.; Adschiri, T.; Arai, K. Conversion of Lignin with Supercritical Water–Phenol Mixtures Energy Fuels **2003**, 17, 922– 928 DOI: 10.1021/ef0202844
28. Brunner, G. Near and Supercritical Water. Part II: Oxidative Processes J. Supercrit. Fluids **2009**, 47, 382– 390 DOI: 10.1016/j.supflu.2008.09.001
29. Brunner, G. Near Critical and Supercritical Water. Part I. Hydrolytic and Hydrothermal Processes J. Supercrit. Fluids **2009**, 47, 373– 381 DOI: 10.1016/j.supflu.2008.09.002
30. Tomai, T.; Tamura, N.; Honma, I. One-Step Production of Anisotropically Etched Graphene Using Supercritical Water ACS Macro Lett. **2013**, 2, 794– 798 DOI: 10.1021/mz400186t
31. Killilea, W. R.; Swallow, K. C.; Hong, G. T. The Fate of Nitrogen in Supercritical-Water Oxidation J. Supercrit. Fluids **1992**, 5, 72– 78 DOI: 10.1016/0896-8446(92)90044-K
32. Peng, J.; Gao, W.; Gupta, B. K.; Liu, Z.; Romero-Aburto, R.; Ge, L.; Song, L.; Alemany, L. B.; Zhan, X.; Gao, G.; Vithayathil, S. A.; Kaipparettu, B. A.; Marti, A. A.; Hayashi, T.; Zhu, J.-J.; Ajayan, P. M. Graphene Quantum Dots Derived from Carbon Fibers Nano Lett. **2012**, 12, 844– 849 DOI: 10.1021/nl2038979
33. Sun, Y.; Wang, S.; Li, C.; Luo, P.; Tao, L.; Wei, Y.; Shi, G. Large Scale Preparation of Graphene Quantum Dots from Graphite with Tunable Fluorescence Properties Phys. Chem. Chem. Phys. **2013**, 15, 9907– 9913 DOI: 10.1039/c3cp50691f
34. Jin, S. H.; Kim, D. H.; Jun, G. H.; Hong, S. H.; Jeon, S. Tuning the Photoluminescence of Graphene Quantum Dots through the Charge Transfer Effect of Functional Groups ACS Nano **2013**, 7, 1239– 1245 DOI: 10.1021/nn304675g
35. Lee, J.; Kim, K.; Park, W. I.; Kim, B.-H.; Park, J. H.; Kim, T.-H.; Bong, S.; Kim, C.-H.; Chae, G.; Jun, M.; Hwang, Y.; Jung, Y. S.; Jeon, S. Uniform Graphene Quantum Dots Patterned from Self-Assembled Silica Nanodots Nano Lett. **2012**, 12, 6078– 6083 DOI: 10.1021/nl302520m
36. Gong, P.; Wang, J.; Sun, W.; Wu, D.; Wang, Z.; Fan, Z.; Wang, H.; Han, X.; Yang, S. Tunable Photoluminescence and Spectrum Split from Fluorinated to Hydroxylated Graphene Nanoscale **2014**, 6, 3316– 3324 DOI: 10.1039/c3nr05725a
37. Galande, C.; Mohite, A. D.; Naumov, A. V.; Gao, W.; Ci, L.; Ajayan, A.; Gao, H.; Srivastava, A.; Weisman, R. B.; Ajayan, P. M. Quasi-Molecular Fluorescence from Graphene Oxide Sci. Rep. **2011**, 1, 885 DOI: 10.1038/srep00085
38. Park, N.-M.; Choi, C.-J.; Seong, T.-Y.; Park, S.-J. Quantum Confinement in Amorphous Silicon Quantum Dots Embedded in Silicon Nitride Phys. Rev. Lett. **2001**, 86, 1355– 1357 DOI: 10.1103/PhysRevLett.86.1355
39. Lu, J.; Boughner, E. C.; Liotta, C. L.; Eckert, C. A. Nearcritical and Supercritical Ethanol as a Benign Solvent: Polarity and Hydrogen-Bonding Fluid Phase Equilib. **2002**, 198, 37– 49 DOI: 10.1016/S0378-3812(01)00754-3
40. Liu, S.; Chen, K.; Fu, Y.; Yu, S.; Bao, Z. Reduced Graphene Oxide Paper by Supercritical Ethanol Treatment and Its Electrochemical Properties Appl. Surf. Sci. **2012**, 258, 5299– 5303 DOI: 10.1016/j.apsusc.2012.02.023
41. Kong, C. Y.; Song, W.-L.; Meziani, M. J.; Tackett, K. N., II; Cao, L.; Farr, A. J.; Anderson, A.; Sun, Y.-P. Supercritical Fluid Conversion of Graphene Oxides J. Supercrit. Fluids **2012**, 61, 206– 211 DOI: 10.1016/j.supflu.2011.09.008
42. Seo, M.; Yoon, D.; Hwang, K. S.; Kang, J. W.; Kim, J. Supercritical Alcohols as Solvents and Reducing Agents for the Synthesis of Reduced Graphene Oxide Carbon **2013**, 64, 207– 218 DOI: 10.1016/j.carbon.2013.07.053
43. Nursanto, E.; Nugroho, A.; Hong, S.; Kim, S.; Chung, K. Y.; Kim, J. Facile Synthesis of Reduced Graphene Oxide in Supercritical Alcohols and Its Lithium Storage Capacity Green Chem. **2011**, 13, 2714– 2718 DOI: 10.1039/c1gc15678k

44. Rangappa, D.; Sone, K.; Wang, M.; Gautam, U. K.; Golberg, D.; Itoh, H.; Ichihara, M.; Honma, I. Rapid and Direct Conversion of Graphite Crystals into High-Yielding, Good-Quality Graphene by Supercritical Fluid Exfoliation Chem. - Eur. J. **2010**, 16, 6488– 6494 DOI: 10.1002/chem.201000199
45. Kumar, S.; McEvoy, N.; Lutz, T.; Keeley, G. P.; Nicolosi, V.; Murray, C. P.; Blau, W. J.; Duesberg, G. S. Gas Phase Controlled Deposition of High Quality Large-Area Graphene Films Chem. Commun. **2010**, 46, 1422– 1424 DOI: 10.1039/b919725g
46. Meyer, J. C.; Geim, A. K.; Katsnelson, M. I.; Novoselov, K. S.; Booth, T. J.; Roth, S. The Structure of Suspended Graphene Sheets Nature **2007**, 446, 60– 63 DOI: 10.1038/nature05545
47. Kosynkin, D. V.; Higginbotham, A. L.; Sinitskii, A.; Lomeda, J. R.; Dimiev, A.; Price, B. K.; Tour, J. M. Longitudinal Unzipping of Carbon Nanotubes to Graphene Nanoribbons Nature **2009**, 458, 872– 876 DOI: 10.1038/nature07872
48. Li, J.; Kudin, K. N.; McAllister, M. J.; Prud'homme, R. K.; Aksay, I. A.; Car, R. Oxygen-Driven Unzipping of Graphitic Materials Phys. Rev. Lett. **2006**, 96, 176101– 176104 DOI: 10.1103/PhysRevLett.96.176101
49. Cruz-Silva, R.; Morelos-Gómez, A.; Vega-Díaz, S.; Tristán-López, F.; Elias, A. L.; Perea-López, N.; Muramatsu, H.; Hayashi, T.; Fujisawa, K.; Kim, Y. A.; Endo, M.; Terrones, M. Formation of Nitrogen-Doped Graphene Nanoribbons *via* Chemical Unzipping ACS Nano **2013**, 7, 2192– 2204 DOI: 10.1021/nn305179b
50. Lim, J.; Maiti, U. N.; Kim, N.; Narayan, R.; Lee, W. J.; Choi, D. S.; Oh, Y.; Lee, J.; Lee, G.; Kang, S. H.; Kim, H.; Kim, Y.; Kim, S. O. Dopant-Specific Unzipping of Carbon Nanotubes for Intact Crystalline Graphene Nanostructures Nat. Commun. **2016**, 7, 10364 DOI: 10.1038/ncomms10364
51. Choucair, M.; Thordarson, P.; Stride, J. A. Gram-Scale Production of Graphene Based on Solvothermal Synthesis and Sonication Nat. Nanotechnol. **2009**, 4, 30– 33 DOI: 10.1038/nnano.2008.365
52. Kuang, Q.; Xie, S. Y.; Jiang, Z. Y.; Zhang, X. H.; Xie, Z. X.; Huang, R. B.; Zheng, L. S. Low Temperature Solvothermal Synthesis of Crumpled Carbon Nanosheets Carbon **2004**, 42, 1737– 1741 DOI: 10.1016/j.carbon.2004.03.008
53. Brooks, J. D.; Taylor, G. H. The Formation of Graphitizing Carbons from the Liquid Phase Carbon **1965**, 3, 185– 193 DOI: 10.1016/0008-6223(65)90047-3
54. Shen, J. M.; Feng, Y. T. Formation of Flower-Like Carbon Nanosheet Aggregations and Their Electrochemical Application J. Phys. Chem. C **2008**, 112, 13114– 13120 DOI: 10.1021/jp802285c
55. Kuijpers, M. W. A.; Iedema, P. D.; Kemmere, M. F.; Keurentjes, J. T. F. The Mechanism of Cavitation-Induced Polymer Scission; Experimental and Computational Verification Polymer **2004**, 45, 6461– 6467 DOI: 10.1016/j.polymer.2004.06.051
56. Lucas, A.; Zakri, C.; Maugey, M.; Pasquali, M.; van der Schoot, P.; Poulin, P. Kinetics of Nanotube and Microfiber Scission under Sonication J. Phys. Chem. C **2009**, 113, 20599– 20605 DOI: 10.1021/jp906296y
57. Odell, J. A.; Keller, A.; Rabin, Y. Flow-Induced Scission of Isolated Macromolecules J. Chem. Phys. **1988**, 88, 4022– 4028 DOI: 10.1063/1.453855
58. Zhang, Z.; Sun, Z.; Yao, J.; Kosynkin, D. V.; Tour, J. M. Transforming Carbon Nanotube Devices into Nanoribbon Devices J. Am. Chem. Soc. **2009**, 131, 13460– 13463 DOI: 10.1021/ja9045923
59. Jiao, L.; Zhang, L.; Wang, X.; Diankov, G.; Dai, H. Narrow Graphene Nanoribbons from Carbon Nanotubes Nature **2009**, 458, 877– 880 DOI: 10.1038/nature07919
60. Wei, D.; Liu, Y.; Zhang, H.; Huang, L.; Wu, B.; Chen, J.; Yu, G. Scalable Synthesis of Few-Layer Graphene Ribbons with Controlled Morphologies by a Template Method and Their Applications in Nanoelectromechanical Switches J. Am. Chem. Soc. **2009**, 131, 11147– 1115 DOI: 10.1021/ja903092k
61. Wu, J.; Becerril, H. A.; Bao, Z.; Liu, Z.; Chen, Y.; Peumans, P. Organic Solar Cells with Solution-Processed Graphene Transparent Electrodes Appl. Phys. Lett. **2008**, 92, 263302– 263308 DOI: 10.1063/1.2924771
62. Becerril, H. A.; Mao, J.; Liu, Z.; Stoltenberg, R. M.; Bao, Z.; Chen, Y. Evaluation of Solution-Processed Reduced Graphene Oxide Films as Transparent Conductors ACS Nano **2008**, 2, 463– 470 DOI: 10.1021/nn700375n
63. Eda, G.; Fanchini, G.; Chhowalla, M. Large-Area Ultrathin Films of Reduced Graphene Oxide as a Transparent and Flexible Electronic Material Nat. Nanotechnol. **2008**, 3, 270– 274 DOI: 10.1038/nnano.2008.83

64. Chakrabarty, A.; Marre, S.; Landis, R. F.; Rotello, V. M.; Maitra, U.; Del Guerzo, A.; Aymonier, C. Continuous Synthesis of High Quality CdSe Quantum Dots in Supercritical Fluids J. Mater. Chem. C **2015**, 3, 7561– 7566 DOI: 10.1039/C5TC01115A